Research Square

Preprints are preliminary reports that have not undergone peer review.
They should not be considered conclusive, used to inform clinical practice,
or referenced by the media as validated information.

Longitudinal Vegetation Configuration Gradients Modulate Hydrodynamics in a Rigid Vegetated Mid-Channel Bar of Braided Rivers

Peng Wang
Wuhan University
Yan Lu
Nanjing Hydraulic Research Institute
Yunshuo Cheng
Wuhan University
Ling Xiong
Wuhan University
Zhiwei Li
lizw2003@whu.edu.cn

Wuhan University https://orcid.org/0000-0002-2870-7265

Research Article

Keywords: braided river, vegetated mid-channel bar, longitudinal vegetation configuration gradient, hydrodynamic processes, flow redistribution

Posted Date: November 23rd, 2026

DOI: https://doi.org/10.21203/rs.3.rs-11570997/v1

License: This work is licensed under a Creative Commons Attribution 4.0 International License.
Read Full License

Longitudinal Vegetation Configuration Gradients Modulate Hydrodynamics in a Rigid Vegetated Mid-Channel Bar of Braided Rivers

Peng Wang[1,2], Yan Lu[2], Yunshuo Cheng[1], Ling Xiong[1], Zhiwei Li[1,*]

[1] State Key Laboratory of Water Resources Engineering and Management, Wuhan University, Wuhan 430072, China

[2] The National Key Laboratory of Water Disaster Prevention, Nanjing Hydraulic Research Institute, Nanjing, 210029, China

* Corresponding author: Zhiwei Li (E-mail: lizw2003@whu.edu.cn)

Abstract: Vegetated mid-channel bars in braided rivers commonly exhibit heterogeneous vegetation distributions, yet the role of longitudinal vegetation configuration in regulating hydrodynamic processes and sediment mobility remains unclear. In this study, an idealized vegetated mid-channel bar model was developed, and nine vegetation configurations, including bare-bar, uniform, positive-gradient, and reverse-gradient cases, were simulated using a three-dimensional numerical approach. The effects of longitudinal vegetation configuration on flow velocity, discharge redistribution, turbulent kinetic energy, bed shear stress, and turbulence-driven sediment entrainment were investigated. Results show that vegetation configuration regulates bar-scale hydrodynamics through the spatial redistribution of vegetation-induced resistance. Vegetation establishment reduced momentum within the vegetated core and diverted flow toward both sides of the elliptical vegetation patch, generating shear layers and high turbulent kinetic energy zones along vegetation boundaries. Increasing positive vegetation gradients concentrated resistance at the bar head, promoting earlier flow adjustment and enhancing downstream recovery, whereas reverse gradients prolonged downstream resistance effects. The strongest positive gradient increased the mean bed shear stress at the bar head by 5.65% but decreased that in the middle and tail regions by 20.05% and 20.98%, respectively, compared with uniform vegetation. The turbulence-based sediment entrainment analysis further revealed that vegetation configuration influenced sediment mobility by modifying the spatial distribution of near-bed turbulent kinetic energy and sediment entrainment potential. These findings highlight that vegetation spatial configuration, rather than vegetation quantity alone, is an important factor controlling hydrodynamic adjustment and sediment stability of vegetated braided-river bars.

Keywords: braided river; vegetated mid-channel bar; longitudinal vegetation configuration gradient; hydrodynamic processes; flow redistribution

1 Introduction

Braided rivers are characterized by multiple channels, active bars, and frequent channel migration [1]. The wide valley reach of the middle Yarlung Tsangpo River on the Tibetan Plateau has a width of 3–5 km and is characterized by wide shallow channels, numerous bifurcations, frequent bar development, and intense aeolian activity. Over the past three decades, windbreak and sand-control measures, together with artificial vegetation restoration, have been implemented along the valley, marginal bars, and parts of mid-channel bars [2]. Vegetation establishment and expansion are jointly influenced by protective barriers, topographic conditions, and restoration strategies [3], while long-term restoration can further modify surface soil grain size and nutrient conditions [4]. In this region, vegetation restoration has increased surface microtopographic roughness by approximately 7.9–16.8 times, indicating that vegetation has become an integral component of the underlying surface structure [5]. Remote sensing analysis of the Qushui–Naidong braided river reach from 1988 to 2021 further revealed that artificial forest coverage has continuously expanded, accompanied by increased average bar area, reduced number of bars, and decreased fragmentation [6]. Therefore, artificial forests not only provide wind and sand control services but have gradually become important ecological and hydrodynamic components that influence flood hydrodynamics, channel bifurcation, and bar boundary stability. Regional-scale numerical simulations further indicate that riparian vegetation can substantially modify flow velocity and bed shear stress [7]. Consequently, understanding how vegetation spatial patterns influence braided-river bar evolution through hydrodynamic alterations has become a key question in ecohydraulic research.

Vegetation and fluvial geomorphology interact through significant bidirectional feedbacks. Flood inundation, bed erosion and deposition, and substrate stability influence plant persistence and expansion, whereas aboveground vegetation drag and belowground root reinforcement modify near-bed flow, sediment transport, and bank erodibility [8-9]. Field observations have demonstrated that vegetation and large wood can trap sediments and facilitate the transition from pioneer bars to stable islands in gravel-bed rivers [10]. Therefore, plants are regarded as ecosystem engineers that influence river structures and processes [11]. Flume experiments have shown that vegetation-induced bank stabilization can reduce the number of active channels and lateral migration rates [12-13]. Numerical

and experimental studies further indicate that vegetation can drive highly dynamic braided rivers toward more stable multi-channel or single-channel configurations [14-15]. These findings have contributed to the "flow-sediment-vegetation-geomorphology" feedback framework [16-17]. However, although the effects of spatially heterogeneous vegetation have received increasing attention, the independent role of longitudinal vegetation configuration remains insufficiently understood, particularly for finite-width vegetated mid-channel bars. Ricardo et al. [18] demonstrated that longitudinal stem-density gradients can influence mean flow and turbulence characteristics, while Yagci et al. [19] further highlighted the hydrodynamic and morphological effects of streamwise vegetation heterogeneity. However, these studies did not specifically isolate the effect of longitudinal vegetation configuration on bar-scale flow responses while maintaining bar geometry, total vegetation quantity, transverse arrangement, and vegetation coverage unchanged. Therefore, how longitudinal vegetation configuration alone redistributes vegetation-induced resistance and regulates bar-scale flow redistribution and turbulence remains unclear.

For emergent rigid vegetation, stems extract momentum from the mean flow through form drag [20]. Vegetation resistance is primarily governed by frontal area density, local flow velocity, and drag coefficient [21-22], while the drag coefficient is further influenced by plant Reynolds number, spatial arrangement, and wake interactions among neighboring plants [23]. Increasing vegetation density therefore enhances the overall blockage effect; however, it also intensifies sheltering effects between upstream and downstream vegetation rows, reducing the effective incoming flow experienced by downstream plants. Consequently, the total resistance does not increase linearly with plant number [24]. Previous studies have further demonstrated that, with identical vegetation quantity, different spatial arrangements can generate distinct hydrodynamic responses by modifying sheltering effects and flow pathways [25]. Existing resistance parameterization approaches can describe the average hydrodynamic effects of uniformly vegetated regions [26-27], whereas the frontal area of branches and leaves and flexible reconfiguration of natural woody vegetation further modify vegetation resistance [28]. Therefore, vegetation density determines the magnitude of local resistance, while plant arrangement regulates the spatial distribution of resistance effects.

Hydrodynamic responses of finite-width vegetation patches differ from those of uniformly vegetated regions extending across the entire flow width. Incoming flow first undergoes pressure adjustment upstream of the patch, followed by deceleration within the patch and diversion toward the adjacent open-water regions. The adjustment length is jointly controlled by patch width, frontal area density, and blockage intensity [29]. Flow velocity inside and outside vegetation patches exhibits an

approximately exponential adjustment along the streamwise direction, with the adjustment rate varying with vegetation density and resistance parameters [30-31]. Lateral flow diversion generates high-velocity zones and transverse velocity gradients along vegetation edges [32]. Once velocity profiles develop inflection points, edge shear layers can induce large-scale coherent structures and enhance lateral momentum exchange between vegetated and open-water regions [33]. The formation and subsequent development of canopy-interface mixing layers further regulate turbulent kinetic energy and exchange scales [34-35]. Downstream of the patch, the central low-velocity wake interacts with high-momentum flows from both sides, while wake structures and recovery distances vary with blockage intensity [36-37]. These mean-flow and turbulent adjustments contribute to spatially varying sediment deposition and erosion patterns within patches, at lateral edges, and in wake regions [38-39], and are further influenced by plant rigidity, flexibility, and local velocity thresholds [40-41]. Previous studies on vegetation spatial configuration have demonstrated that average vegetation density alone cannot fully characterize patch-scale hydrodynamics. In regular arrays, variations in longitudinal and transverse plant spacing can produce different resistance responses [25]. Under identical vegetation coverage, staggered arrangements exhibit substantially greater hydraulic resistance than aligned arrangements [42]. Density contrasts between adjacent patches modify wake interactions and turbulent recovery processes [43], whereas the blockage ratio between patch width and channel width influences the intensity of leading-edge flow diversion [44]. Dynamic patch experiments further reveal that local flow conditions and sediment feedback can, in turn, modify vegetation patch morphology [45]. Recent studies of nearshore finite vegetation patches have further highlighted pronounced spatial heterogeneity in the downstream adjustment of mean flow and turbulence [46]. However, these studies have mainly focused on variations in overall density, lateral contraction ratio, coverage, patch number, or arrangement patterns. For vegetated mid-channel bars, natural vegetation expansion is rarely uniform; instead, spatial heterogeneity arises from pioneer vegetation establishment at bar heads, sediment accumulation at bar tails, and flood disturbances. Therefore, longitudinal vegetation configuration has significant ecological and hydrodynamic implications.

To address this issue, this study selects a typical artificial-forest vegetated mid-channel bar in the middle reaches of the Yarlung Tsangpo River on the Tibetan Plateau as a reference case and develops an idealized numerical model. While the bar geometry, total plant number, transverse arrangement, and vegetation coverage are maintained identical, only the streamwise plant spacing of the artificial forest is varied to establish longitudinal vegetation configuration gradients with different magnitudes and directions. The effects of longitudinal vegetation configuration on bar-scale

hydrodynamics are systematically investigated by analyzing mean flow velocity, turbulent kinetic energy, bed shear stress, and flow redistribution. The objective of this study is to distinguish the effects of vegetation amount from those of spatial configuration, reveal the mechanism by which longitudinal vegetation gradients regulate bar hydrodynamic responses through the spatial redistribution of vegetation-induced resistance, and provide hydrodynamic insights for evaluating the stability of vegetated bars in braided rivers.

2 Materials and Methods

2.1 Model Conceptualization

The braided rivers in the middle reaches of the Yarlung Tsangpo River on the Tibetan Plateau are characterized by wide and shallow channels, multiple bifurcations, and frequent bar evolution. Vegetated mid-channel bars have gradually become important geomorphic units influencing channel hydrodynamic adjustment and bar stability (Fig. 1a). In this study, a typical vegetated mid-channel bar in this region was selected as a reference case, and its spatial morphology and vegetation distribution characteristics were characterized based on remote sensing images, UAV observations, and field survey data (Fig. 1b). Natural mid-channel bars are shaped by long-term water and sediment processes and exhibit complex irregular boundaries and heterogeneous vegetation structures. Therefore, directly representing natural morphology makes it difficult to distinguish the effects of vegetation amount from those of spatial configuration. To overcome this limitation, an idealized conceptual model was developed to investigate the mechanism by which longitudinal vegetation configuration gradients influence hydrodynamic processes. The planform geometry of the mid-channel bar was idealized as an elliptical shape extending in the streamwise direction. A fixed-bed condition was adopted for the geometric boundary, and regularly arranged rigid cylinders were used to represent the stems of emergent vegetation (Fig. 1c). The bar length, width, total number of plants, transverse arrangement, and vegetation coverage were kept constant, while only the streamwise plant spacing distribution was modified. This approach allowed the effects of vegetation spatial configuration to be isolated from those of vegetation amount. Based on the longitudinal variation characteristics of artificial forests in natural settings, the mid-channel bar was divided into three regions: the bar head (Head, H), middle region (Middle, M), and bar tail (Tail, T). Different vegetation configuration gradients were established by adjusting the streamwise plant spacing within these three regions.

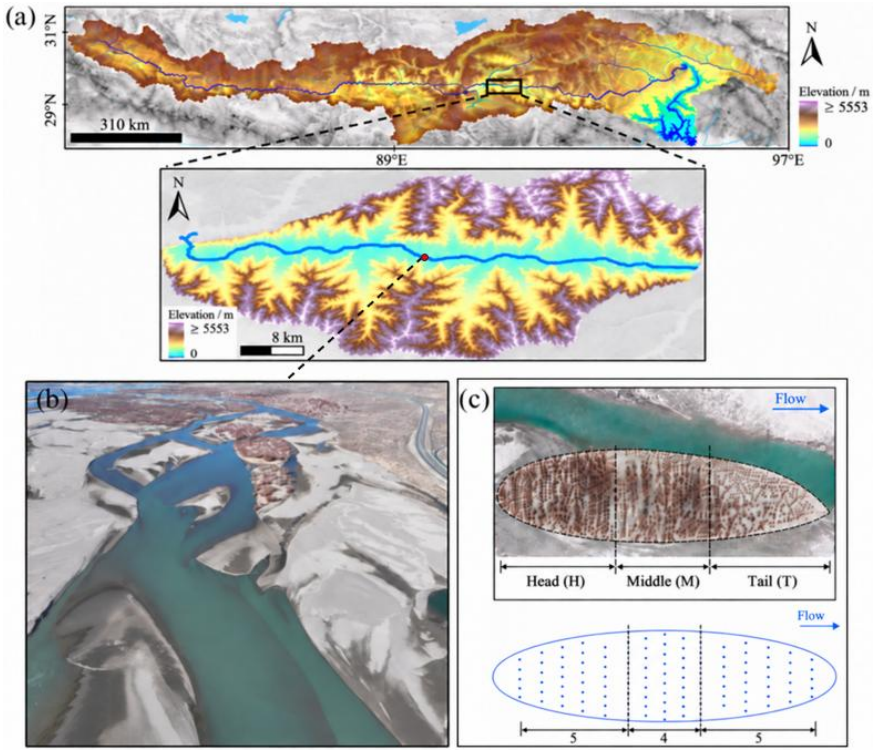

Fig. 1 Reference case of a vegetated mid-channel bar in the middle reaches of the Yarlung Tsangpo River on the Tibetan Plateau and conceptual model development. (a) Location of the study area and representative braided river reach; (b) UAV image of a typical vegetated mid-channel bar in December 2025; (c) Reference case of the vegetated mid-channel bar and conceptual numerical model, where H, M, and T represent the bar head, middle region, and bar tail, respectively.

2.2 Computational Domain and Case Design

The computational domain consisted of a straight horizontal-bed flume with a length of L = 20.0 m and a width of B =1.20 m. The origin of the coordinate system was defined at the lower-left corner of the inlet bed, where x, y, and z denote the streamwise, transverse, and vertical coordinates, respectively, and the z-axis is oriented vertically upward. The mid-channel bar was positioned in the central region of the flume and within the vegetation-affected zone along the streamwise direction, ensuring that the computational domain captured vegetation-induced leading-edge flow adjustment, internal flow deceleration, and wake recovery processes. The bar head and bar tail were located at x_h = 6.0 m and x_t = 8.0 m, respectively, and the planform center was located at (7.0 m, 0.60 m). The bar length, maximum width, and maximum height were L_b = 2.0 m, B_b = 0.60 m, and H_b = 0.060 m, respectively. The computational domain and model configuration are shown in Fig. 2. The

177 reference water depth was H_0 = 0.12 m, and the inlet cross-sectional mean velocity was U_0 = 0.24
178 m/s. The Froude number based on water depth was 0.22, indicating subcritical flow conditions. The
179 plant diameter was d =0.012 m, with 15 rows arranged in the streamwise direction and a total of 110
180 plants. The transverse spacing was fixed at S_y = 0.060 m = 5d, and adjacent rows were arranged in a
181 staggered pattern with a half-spacing offset (Δy = 0.030 m).

182 To characterize the longitudinal variation in vegetation spatial configuration, the streamwise
183 plant spacing was divided into three regions: the bar head (Head, H), middle region (Middle, M), and
184 bar tail (Tail, T). The bar head and bar tail each consisted of five longitudinal spacing units, whereas
185 the middle region contained four longitudinal spacing units. These three regions corresponded to
186 average longitudinal spacings of S_H , S_M and S_T , respectively. To maintain a consistent vegetation
187 structure in the middle region, the spacing in this region was fixed at S_M = 0.120 m. Different
188 longitudinal vegetation configuration gradients were generated by adjusting the spacing in the bar
189 head and bar tail regions. A dimensionless parameter λ was introduced to quantify the longitudinal
190 vegetation configuration gradient：

191 $$\lambda = \frac{S_T - S_H}{2S_M} \tag{1}$$

192 $$S_H = S_M(1-\lambda) \tag{2}$$

193 $$S_T = S_M(1+\lambda) \tag{3}$$

194 where $\lambda > 0$ represents a smaller vegetation spacing at the bar head and a larger vegetation spacing
195 at the bar tail, corresponding to a gradual transition from dense to sparse vegetation; $\lambda < 0$
196 represents a larger vegetation spacing at the bar head and a smaller vegetation spacing at the bar tail,
197 corresponding to a transition from sparse to dense vegetation; and $\lambda = 0$ represents a uniform
198 vegetation distribution along the streamwise direction.

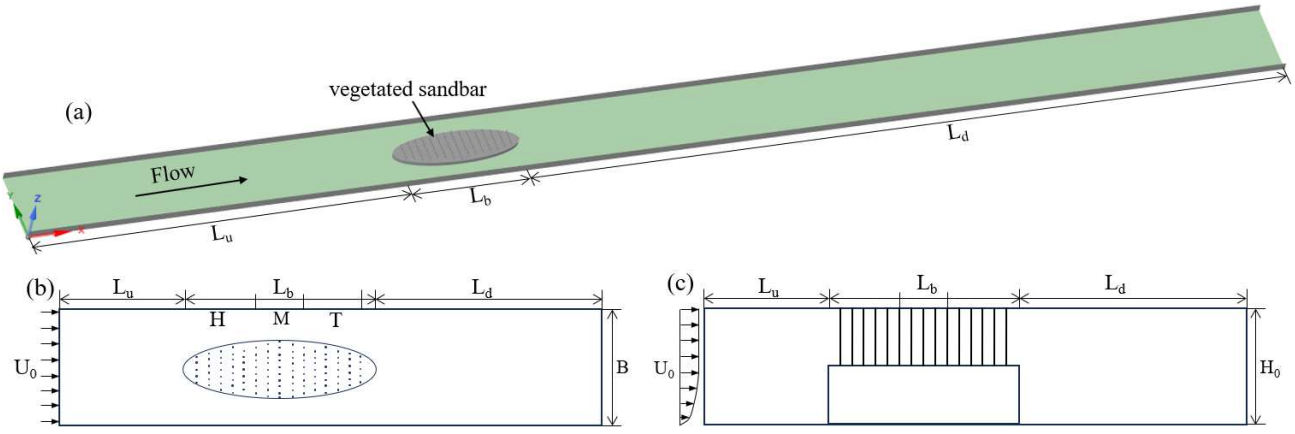

Fig. 2 Schematic illustration of the numerical model. (a) Three-dimensional view; (b) top view; (c) side view.

Nine computational cases were considered, including the bare-bar case B, the uniformly vegetated case G0, six positive longitudinal vegetation configuration gradient cases (G1–G6), and the reverse-gradient case GR (Table 1). The bare-bar case B was used to evaluate the additional hydrodynamic effects introduced by vegetation, G0–G6 were used to investigate the effects of longitudinal vegetation configuration gradient intensity, and GR was used to examine the influence of gradient direction under an identical gradient magnitude.

Table 1 Computational cases and longitudinal vegetation spacings

Case	S_H (mm)	S_M (mm)	S_T (mm)	λ
B	—	—	—	—
G0	120	120	120	0
G1	108	120	132	0.1
G2	96	120	144	0.2
G3	84	120	156	0.3
G4	72	120	168	0.4
G5	60	120	180	0.5
G6	48	120	192	0.6
GR	168	120	72	−0.4

2.3 Numerical Method and Boundary Conditions

This study focuses on the mean hydrodynamic structures and their spatial responses under different longitudinal vegetation configurations rather than transient vortex evolution. Therefore, the

three-dimensional Reynolds-averaged Navier–Stokes (RANS) equations were solved using the shear stress transport (SST) k–ω turbulence model. The SST model combines the advantages of the k–ω formulation near solid boundaries and the k–ε formulation in free-shear regions, enabling the representation of vegetation-induced flow separation, shear-layer development, and wake recovery processes. Vegetation elements were explicitly represented by rigid cylindrical structures rather than simplified resistance-source terms. This approach allows direct resolution of flow separation and wake development around individual stems. The numerical simulations were performed using a pressure-based solver. The pressure–velocity coupling was achieved using the SIMPLE algorithm, and the momentum and turbulence transport equations were discretized using second-order spatial schemes.

To minimize the additional influence of an idealized uniform inlet condition on the upstream flow adjustment of the mid-channel bar, a unified periodic precursor flow field was generated and applied as the inlet condition for all primary simulations. The precursor simulation employed the same flume cross-section as the main computational domain, without including the mid-channel bar and vegetation elements. Periodic boundary conditions were applied in the streamwise direction. After the flow field became fully developed and reached a statistically stable state, the spatial distributions of the three velocity components u, v and w, together with turbulent kinetic energy and specific dissipation rate, were extracted at the $x = 15$ m section. These distributions were subsequently mapped to the inlet boundary and used as inlet conditions for all main simulations. This approach ensured identical incoming flow conditions among different vegetation configurations, allowing the differences between cases to be primarily attributed to the longitudinal vegetation configurations. A pressure outlet boundary condition was applied at the outlet. The flume bed, sidewalls, mid-channel bar surface, and cylindrical vegetation surfaces were treated as no-slip solid boundaries. Because the simulated conditions corresponded to low-Froude-number subcritical flow ($Fr = 0.22$), and the focus of this study was on vegetation-induced mean flow structures, turbulence responses, and bed shear variations rather than free-surface fluctuations, the free surface was treated using a rigid-lid assumption. Zero normal velocity and zero tangential shear stress were imposed at the free surface.

2.4 Mesh Setup and Numerical Validation

A Poly-Hexcore unstructured hybrid mesh was generated using Fluent Meshing. Because the flow around cylindrical vegetation elements, shear-layer development along bar edges, and wake recovery processes involve strong velocity gradients, a regionally refined mesh strategy was adopted. Relatively coarse meshes were applied in regions outside the vegetation-affected zone to reduce

computational cost, whereas local refinement was implemented in the vegetated mid-channel bar region, upstream bar-head region, bar margins, and near-wake recovery zone to adequately resolve the key hydrodynamic processes. The maximum mesh size within the vegetated mid-channel bar region was limited to 4 mm, while further refinement was applied to the bar-head region, bar margins, and near-wake region with a mesh size of 2 mm. Local refinement was also applied around the cylindrical vegetation surfaces, with a minimum mesh size of 1.0 mm, to capture vegetation-scale flow separation and wake structures. Ten prism layers were generated adjacent to solid boundaries, with the first-layer thickness set to 0.05 mm and a growth rate of 1.20, improving the resolution of near-wall velocity gradients and bed shear stress calculations. The same mesh generation criteria were applied to all cases, resulting in approximately 6 million cells for the final computational mesh. A mesh independence analysis was performed using the G6 case, which exhibited the strongest longitudinal vegetation gradient. Three mesh resolutions were considered, with approximately 3.1 million, 6.0 million, and 11 million cells. The average velocity in the bar-head central region, center-flow ratio, and average bed shear stress at the bar head were selected as evaluation parameters. With increasing mesh resolution, all parameters gradually approached stable values. The relative differences between the 6.0 million-cell and 11 million-cell meshes were below 0.3%, and the streamwise velocity distributions and flow redistribution patterns remained consistent. Therefore, considering both computational accuracy and efficiency, approximately 6 million cells were adopted for all subsequent simulations.

To further evaluate the capability of the numerical model in reproducing vegetation-induced mean-flow and turbulence characteristics, two sets of available flume experimental data were employed for validation. First, the finite emergent vegetation patch experiment conducted by Zong and Nepf [37] was used to validate the wake-flow characteristics behind a vegetation patch. As shown in Figure 3(a), the numerical result reproduced the streamwise variation of normalized centerline velocity. The rapid velocity reduction immediately downstream of the vegetation patch and the subsequent gradual recovery were well captured. Second, the vegetated mid-channel bar experiment conducted by Nandi et al. [47] was employed to further validate the model under more complex bar-scale flow conditions. Figures 3(b) and 3(c) compare the experimental and numerical vertical profiles of normalized streamwise velocity and dimensionless turbulent kinetic energy, respectively, at three representative cross-sections (CS1–CS3). The numerical results generally reproduced the vertical variation in streamwise velocity at all three cross-sections, including the characteristic velocity adjustment within the lower and middle parts of the flow depth. For turbulent kinetic energy, the

simulations captured the main vertical variation and the locations of enhanced turbulence observed in the experiments, although some local discrepancies remained in the peak magnitudes. Overall, the comparisons demonstrate that the numerical model can reasonably reproduce both the mean-flow structure and turbulence characteristics of flow over a vegetated mid-channel bar.

In summary, the mesh independence analysis and comparisons with the two experimental datasets demonstrate that the proposed numerical model can reasonably reproduce vegetation-induced mean-flow adjustment, wake recovery, velocity fluctuations, and turbulent kinetic energy distributions. Therefore, the developed model provides a reliable basis for investigating the relative hydrodynamic and turbulence responses associated with different longitudinal vegetation configurations.

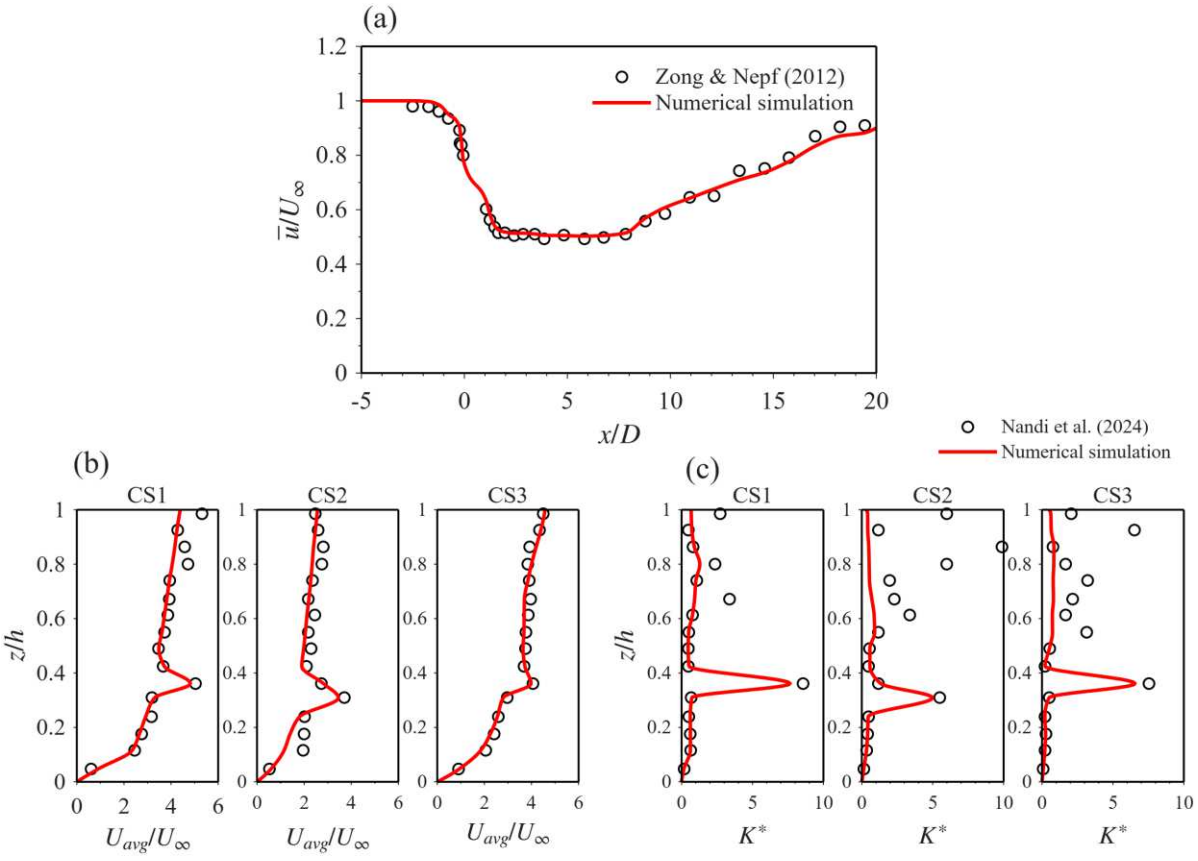

Fig. 3 Validation of the numerical model against experimental measurements. (a) Streamwise variation of normalized centerline velocity of a finite emergent vegetation patch based on the experiments of Zong and Nepf [37]; (b) vertical profiles of normalized streamwise velocity and (c) dimensionless turbulent kinetic energy at three representative cross-sections (CS1–CS3) of a vegetated mid-channel bar based on the experiments of Nandi et al. [47].

3 Results and Analysis

3.1 Spatial Characteristics of Flow Structure

3.1.1 Streamwise Velocity Distribution

The flow structures around the vegetated mid-channel bar were strongly influenced by both vegetation presence and its longitudinal configuration. Figure 4 presents the spatial distributions of dimensionless streamwise velocity U^* near the water surface ($Z^* = 0.75$) and in the near-bed region ($Z^* = 0.25$) under different vegetation configurations. In general, vegetation substantially modified the velocity distribution compared with the bare-bar condition. The high-velocity zones shifted from the bar crest toward the lateral flow-conveyance regions, forming a low-velocity core within the vegetated area and accelerated flow along both sides.

In the near-surface region (Fig. 4a), the bare-bar case B exhibited relatively high velocities over the bar crest, with the local velocity reaching approximately 1.3. However, flow expansion and separation near the bar tail generated a velocity-deficit region, where the minimum velocity decreased to approximately 0.4. After introducing uniform vegetation (G0), vegetation resistance enhanced momentum dissipation within the central region, forming a continuous low-velocity zone over the vegetated area, whereas the lateral open-water regions maintained relatively high velocities that locally exceeding 1.2. With increasing positive longitudinal vegetation configuration gradients (G0–G6), the velocity-deficit region gradually migrated toward the bar head. In the G6 case, the central velocity near the bar head decreased to below 0.4, whereas the lateral high-velocity zones remained approximately 1.3, suggesting that stronger gradients mainly changed the location of velocity adjustment rather than continuously increasing velocity differences. In the near-bed region (Fig. 4b), the near-bed velocity distribution exhibited similar characteristics, with vegetation producing a low-velocity band downstream of stems and maintaining relatively high velocities near the lateral margins. The central near-bed velocity decreased to approximately 0.3–0.4 after vegetation introduction, while lateral velocities remained above 1.2. In contrast, the reverse-gradient case GR shifted dense vegetation toward the bar tail, extending the low-velocity region downstream and delaying velocity recovery. These results indicate that longitudinal vegetation configuration regulates velocity redistribution by changing the spatial distribution of vegetation resistance. Dense vegetation at the bar head promotes early flow adjustment, whereas sparse downstream vegetation reduces persistent resistance and facilitates recovery.

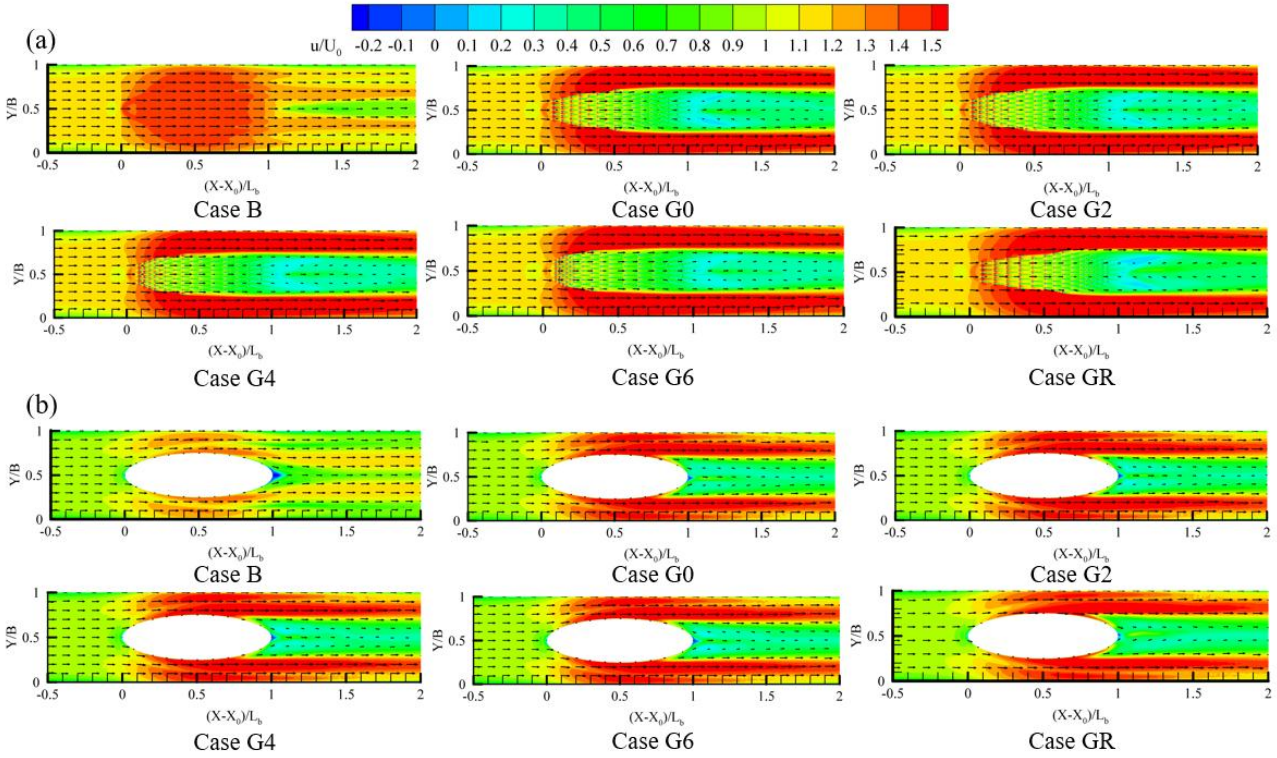

Fig. 4 Spatial distributions of dimensionless streamwise velocity U^* under different vegetation configurations: (a) near-surface plane (Z^* = 0.75); (b) near-bed plane (Z^* = 0.25).

3.1.2 Spatial adjustment of longitudinal velocity

To quantitatively evaluate the effects of different longitudinal vegetation configurations on velocity adjustment in the central flow region, the mean velocity within the central band was selected as the longitudinal velocity response parameter. Specifically, the streamwise velocity was averaged over a central band with a transverse width of 0.6 m to characterize the longitudinal momentum variation under different vegetation configurations. Figure 5 presents the longitudinal evolution of central-band dimensionless streamwise velocity and the corresponding characteristic velocities at the bar-head and near-wake regions. Before the flow entered the influence zone of the mid-channel bar, all cases exhibited nearly identical velocity distributions, confirming the consistency of inlet flow conditions. After entering the bar-head region, velocity responses gradually diverged, indicating distinct flow adjustment processes induced by different vegetation arrangements.

The bare-bar case B primarily reflects the hydrodynamic effects of bar morphology. Due to flow contraction around the mid-channel bar, the central-band velocity increased continuously near the bar head and reached approximately U_C^* = 1.46 above the bar surface, followed by a gradual decrease

caused by flow expansion and separation downstream of the bar. After vegetation was introduced, the velocity evolution pattern was substantially modified. For the uniformly vegetated case G0, the central-band velocity decreased rapidly after entering the bar-head region and reached its minimum value within the downstream wake region, indicating continuous momentum extraction by vegetation resistance. The positive vegetation gradients (G0–G6) mainly affected the spatial distribution of velocity adjustment. At the bar head (X^* = 0.05), the U_C^* values of G0, G2, G4, and G6 were approximately 1.278, 1.269, 1.261, and 1.245, respectively. Relative to G0, the corresponding reductions in velocity for G2, G4, and G6 were approximately 0.7%, 1.3%, and 2.6%. As vegetation spacing decreased at the bar head, the frontal projected area density increased, strengthening the resistance effect and causing earlier flow deceleration and lateral diversion within the vegetated zone. Within the bar interior, the central velocity continued to decrease for all vegetated cases, while the differences among configurations did not continuously increase in the downstream direction. Further downstream, however, the velocity responses among different gradient configurations gradually diverged in the opposite trend. At the near-wake location (X^* = 1.05), the U_C^* values of G0, G2, G4, and G6 were approximately 0.361, 0.373, 0.388, and 0.401, respectively. Compared with G0, these values increased by approximately 3.3%, 7.5%, and 11.1%, respectively. This indicates that although positive gradients enhance resistance-induced deceleration near the bar head, the increased vegetation spacing downstream reduces persistent resistance, facilitating momentum exchange from the high-speed side regions toward the wake center and accelerating velocity recovery.

Figure 5(b) compares the differences in central-band velocity between the bar-head and near-wake locations. For G0, the velocity decreased from 1.278 at the bar head to 0.361 in the near wake, corresponding to a velocity attenuation of 71.8%. For G6, the velocity decreased from 1.245 to 0.401, with the attenuation reduced to 67.8%, approximately 4% lower than that of G0. This indicates that stronger positive gradients redistribute velocity loss toward the upstream adjustment region and enhance downstream velocity recovery. The effect of gradient direction was further examined by comparing G4 and GR. Under identical gradient magnitudes, the near-wake central velocities were approximately 0.388 and 0.344 for G4 and GR, respectively, with G4 exhibiting a 12.8% higher velocity. Although both cases contained identical vegetation quantities and overall density, different locations of high-resistance zones resulted in distinct velocity recovery patterns. In G4, dense vegetation located at the bar head promoted earlier flow adjustment, whereas in GR, dense vegetation shifted toward the bar tail maintained downstream resistance and inhibited wake recovery.

Collectively, longitudinal vegetation gradients regulate central-flow velocity evolution through spatial redistribution of vegetation resistance. Positive gradients produce early adjustment at the bar head and enhanced recovery downstream, whereas reverse gradients extend the influence of resistance toward the downstream region.

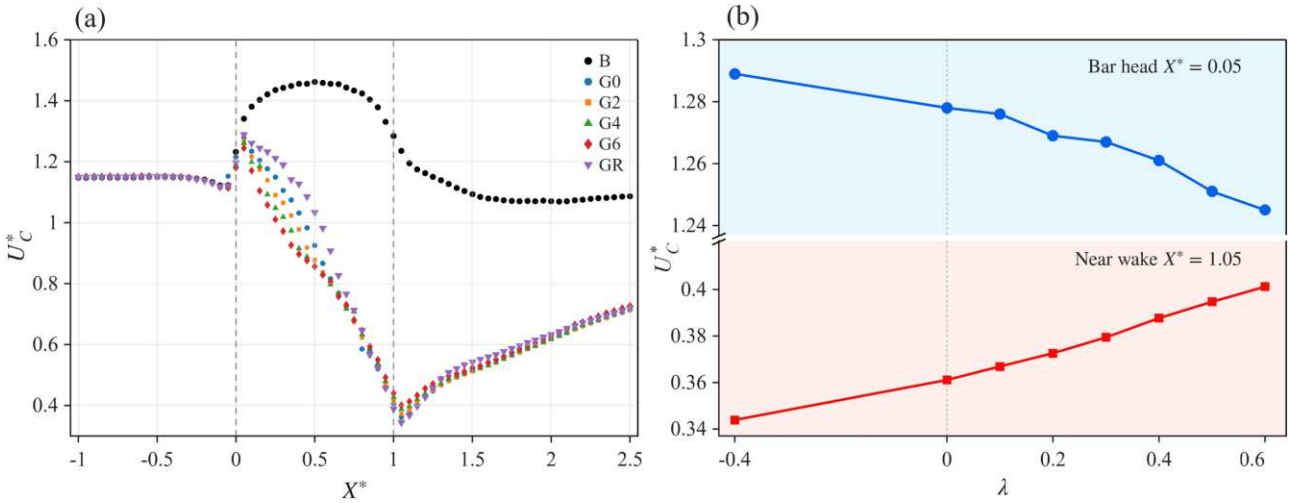

Fig. 5 Longitudinal adjustment of the central-band dimensionless streamwise velocity under different vegetation configurations. (a) Streamwise evolution of central-band velocity; (b) Comparison of central-band velocity at the bar-head and near-wake locations.

3.1.3 Flow redistribution induced by the rigid vegetation

Longitudinal vegetation configuration alters the streamwise redistribution of discharge by modifying the spatial distribution of vegetation-induced resistance. Figure 6 presents the longitudinal variation of the central flow ratio and its sensitivity to longitudinal vegetation configuration gradients under different vegetation arrangements. Here, α_C represents the proportion of discharge passing through the central region of the mid-channel bar, while S_λ quantifies the response of the central flow ratio to variations in the longitudinal vegetation configuration gradients. The flow redistribution characteristics were evaluated at four representative locations: upstream of the bar, the bar-head region, the central bar region, and the downstream near-wake region. Before entering the influence zone of the mid-channel bar (X^* = -0.30), all cases exhibited nearly identical central flow ratios, with an average value of approximately 0.523. This confirms that all vegetation configurations experienced the same initial flow partitioning conditions. Once the flow entered the bar region, vegetation resistance combined with the geometric constriction of the bar induced a progressive transfer of discharge from the central region toward the lateral flow-conveyance pathways. At the

initial adjustment location near the bar head (X^* = 0.05), distinct differences were already observed among different configurations. The central flow ratios for B, GR, G0, G2, G4, and G6 were approximately 0.458, 0.445, 0.443, 0.440, 0.438, and 0.434, respectively. Compared with the bare-bar condition, vegetation reduced the central flow ratio by approximately 3.3%, indicating that vegetation resistance enhanced momentum dissipation within the central region and promoted lateral flow redistribution. However, the decrease from G0 to G6 was only approximately 2.1%, suggesting that once the initial redistribution process was established, further increases in bar-head resistance produced diminishing effects on central flow partitioning. Further downstream, the difference in central flow ratios among different gradient configurations reached its maximum at (X^* = 0.35).

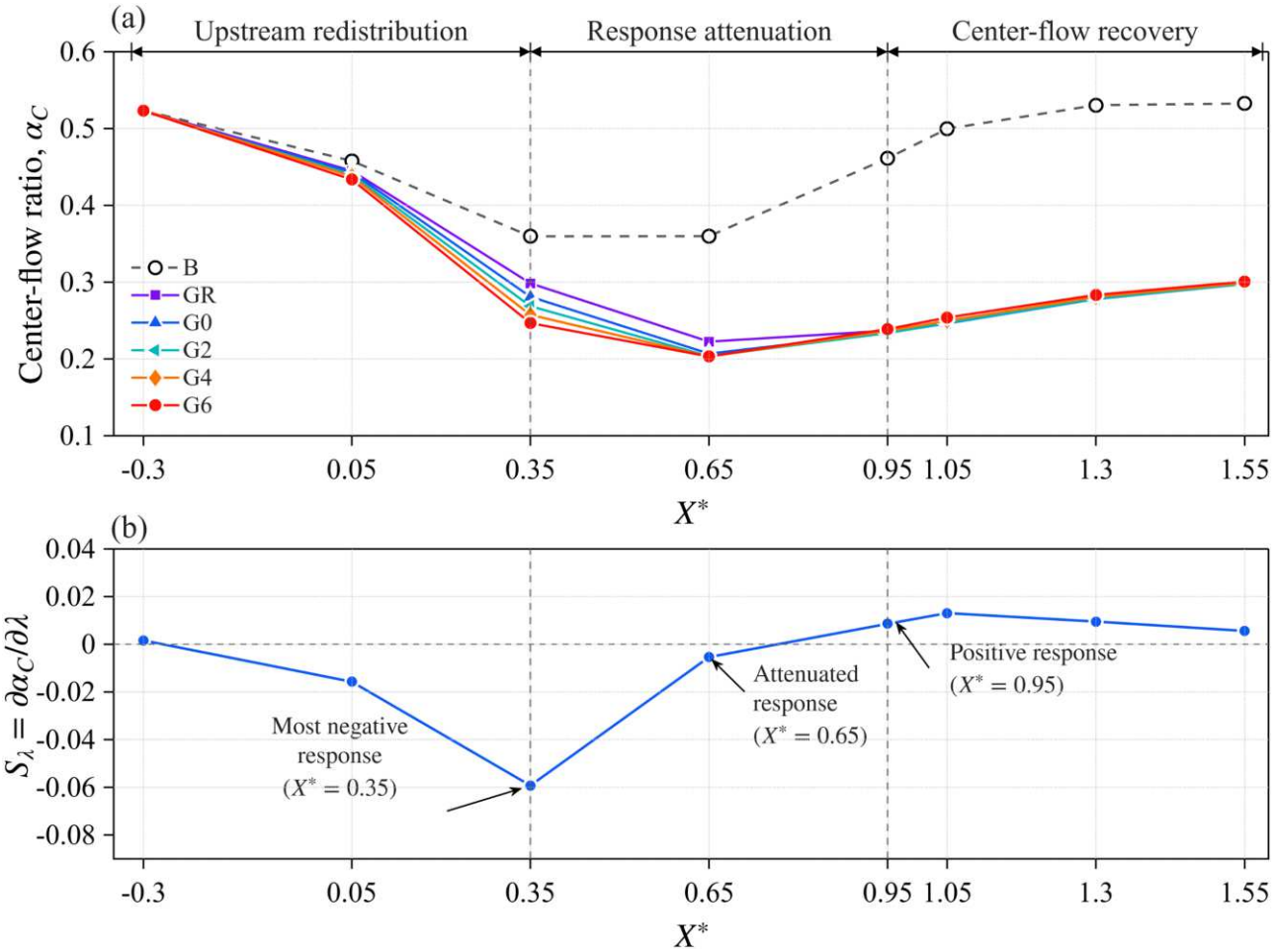

Fig. 6 Longitudinal variations in the central flow ratio under different vegetation configurations: (a) streamwise variation of the central flow ratio α_C; (b) streamwise variation of the gradient sensitivity S_λ of α_C.

412 The sensitivity analysis further clarifies the streamwise location at which vegetation
413 configuration exerts its strongest influence on flow redistribution. Figure 6(b) indicates that this
414 position corresponds to the minimum gradient sensitivity (S_Γ = -0.059), demonstrating that the
415 central flow ratio exhibits the strongest response to changes in longitudinal vegetation configuration
416 at this location. The enhanced positive gradient further reduced the central flow ratio, indicating that
417 the resistance generated by dense vegetation at the bar head required a certain downstream
418 development distance before producing its strongest impact on lateral discharge redistribution.
419 Within the response attenuation region in the middle part of the bar (X^* = 0.65), differences among
420 configurations gradually decreased. The gradient sensitivity decreased to approximately −0.005,
421 indicating that differences in flow adjustment among vegetation configurations became considerably
422 weaker. After passing through the upstream resistance adjustment region, discharge partitioning
423 between the central and lateral regions gradually approached a stable state, and further increases in
424 bar-head vegetation density exerted limited influence on flow redistribution. When the flow entered
425 the near-wake recovery region (X^* = 0.95), the variation trend of the central flow ratio changed.
426 Positive-gradient configurations exhibited recovery of the central flow ratio, and the recovery
427 magnitude increased with increasing gradient intensity. Compared with G0, the increases in central
428 flow ratio for G1–G6 were approximately 0.00025, 0.00049, 0.00194, 0.00347, 0.00557, and 0.00768,
429 respectively, with G6 exhibiting the largest recovery. This recovery was mainly attributed to the
430 increased vegetation spacing at the bar tail under positive gradients, which weakened downstream
431 resistance and enhanced momentum exchange between lateral high-speed flows and the central wake
432 region. Gradient direction further influenced the flow redistribution pathway. Although G4 and GR
433 contained identical vegetation quantities under the same gradient magnitude, their longitudinal
434 response patterns differed substantially. In G4, dense vegetation located at the bar head caused the
435 major redistribution process to occur upstream, allowing faster flow recovery downstream.
436 Conversely, GR shifted dense vegetation toward the bar tail, extending the resistance effect
437 downstream and restricting recovery of the central flow ratio.
438 Overall, the influence of longitudinal vegetation configuration gradients on flow redistribution
439 exhibits distinct spatial response stages. The upstream region corresponds to the initial flow diversion
440 response, the intermediate region represents the maximum gradient effect, the downstream region
441 shows gradual response attenuation, and the near-wake region corresponds to central-flow recovery.
442 These results demonstrate that longitudinal vegetation configurations regulate both the location of

discharge redistribution and the subsequent recovery pathway by modifying the spatial distribution of vegetation-induced resistance.

3.2 Turbulent kinetic energy distribution

In addition to modifying the mean-flow structure, longitudinal vegetation configuration also regulates the spatial distribution of turbulence around the vegetated mid-channel bar. Figure 7 illustrates the spatial distributions of dimensionless turbulent kinetic energy k^* near the water surface (Z^* = 0.75) and near the bed (Z^* = 0.25) under different longitudinal vegetation configurations. Under bare-bar conditions, turbulent kinetic energy was primarily associated with flow acceleration around the bar margins, flow convergence near the bar tail, and local velocity gradients. Following vegetation introduction, stem-scale wake formation, vegetation-edge shear layers, and downstream wake recovery jointly controlled the spatial distribution of turbulent kinetic energy. With varying longitudinal vegetation gradients, turbulent kinetic energy exhibited pronounced spatial redistribution rather than a uniform increase throughout the flow field. At the near-surface level (Figure 7a), high turbulent kinetic energy zones in case B were mainly located near the bar-tail convergence region and lateral bar margins, with maximum values of approximately 0.015-0.020, whereas most areas within the bar interior remained at relatively low levels (k^* < 0.010). After introducing uniform vegetation (G0), stem-induced wake structures and enhanced shear layers expanded high turbulent kinetic energy regions from the downstream convergence zone to the vegetation leading edge, lateral vegetation boundaries, and wake regions. The vegetation front and lateral shear zones near the bar head reached values of approximately 0.035–0.050, representing an increase of approximately 1–2 times compared with the maximum value under bare-bar conditions. Meanwhile, the central vegetated region maintained relatively low turbulent kinetic energy values (approximately 0.010–0.020) due to flow deceleration.

These results indicate that vegetation resistance enhances local turbulence production by increasing velocity gradients. With increasing positive vegetation gradients (G0–G6), the high turbulent kinetic energy regions progressively shifted toward the bar head. Under G0, elevated turbulent kinetic energy occurred near both the bar head and the bar tail. However, in G6, the reduced vegetation spacing at the bar head (from 120 mm to 48 mm) substantially increased the frontal projected area density, producing a more continuous high-turbulence zone along the leading edge and lateral shear regions, where local values reached approximately 0.050–0.060. Conversely, the increased vegetation spacing at the bar tail (192 mm) weakened vegetation resistance and reduced turbulent kinetic energy in the wake region to approximately 0.015–0.025. These results demonstrate

that positive vegetation gradients primarily modify the spatial distribution of turbulence production. Under the same gradient magnitude, G4 exhibited high turbulent kinetic energy mainly around the bar head and the lateral boundaries of the upstream-to-middle vegetation regions, with local values of approximately 0.045–0.055, while most downstream regions remained below 0.025. In contrast, the higher vegetation density at the bar tail in GR resulted in weaker turbulence enhancement near the bar head (approximately 0.020–0.030) but generated continuous high-value regions in the middle-to-downstream and wake regions, with local values reaching approximately 0.045. This comparison confirms that gradient direction determines the position of high-resistance zones and subsequently controls the distribution of turbulence production.

At the near-bed level (Figure 7b), turbulent kinetic energy exhibited stronger spatial localization. In case B, near-bed turbulence was mainly concentrated around the bar margins and the downstream region, with a maximum value of approximately 0.015. After vegetation introduction (G0), stem wakes became the dominant source of turbulence, producing discrete high-value regions downstream of individual stems, with local values increasing to approximately 0.030–0.040. With increasing positive gradients, dense vegetation at the bar head in G6 generated a continuous high-turbulence zone, where local values exceeded approximately 0.045. Meanwhile, increased vegetation spacing at the bar tail weakened wake disturbances, reducing turbulent kinetic energy in the wake region to approximately 0.015-0.020. In contrast, the GR configuration shifted the enhanced near-bed turbulence region downstream because dense vegetation was located at the bar-tail region. Compared with G4, turbulent kinetic energy near the bar head remained lower, whereas the vegetated downstream region maintained relatively high values, locally reaching approximately 0.040-0.050. This indicates that the direction of longitudinal vegetation configuration regulates the spatial extent of near-bed turbulence.

In summary, the effect of longitudinal vegetation gradients on turbulent kinetic energy is primarily manifested through spatial redistribution. Positive gradients enhance frontal velocity gradients through dense vegetation at the bar head, promoting earlier turbulence production and reducing persistent downstream disturbances. Conversely, reverse gradients shift high turbulent kinetic energy regions toward the middle and downstream regions, thereby strengthening turbulence within the wake region.

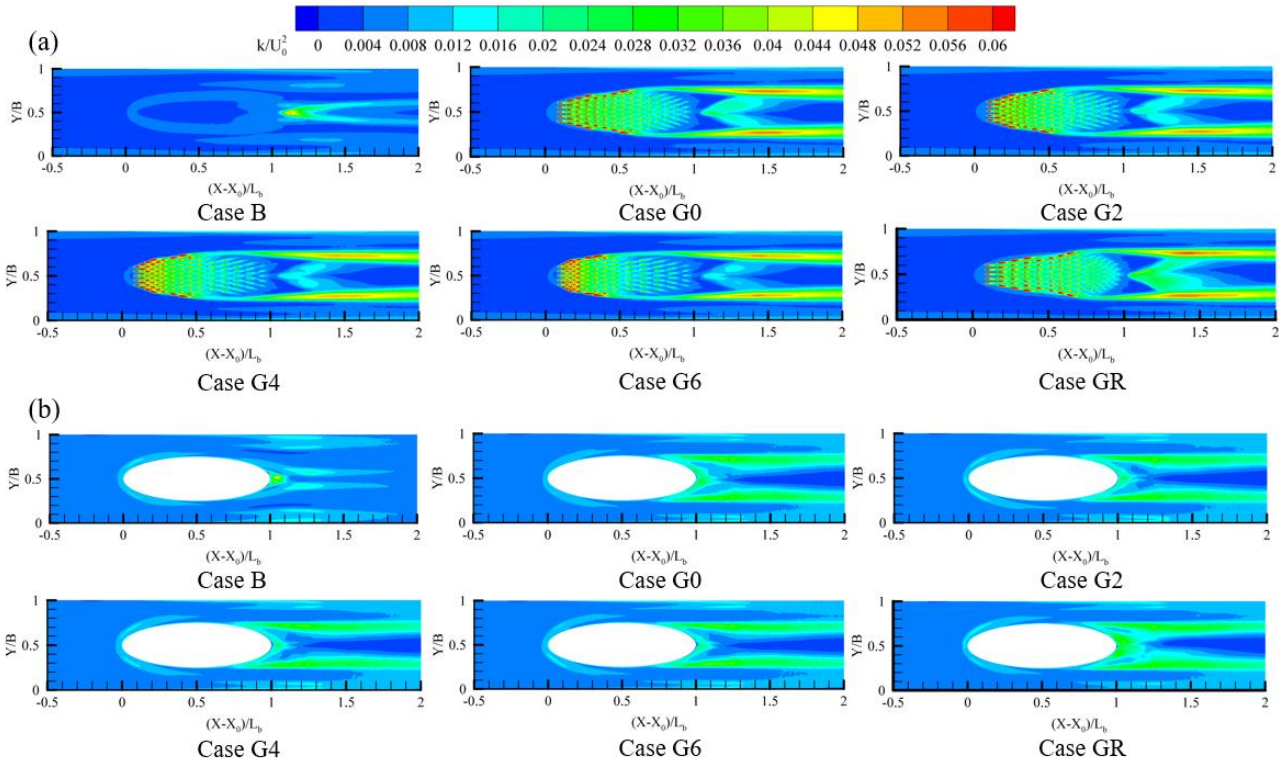

Fig. 7 Distributions of dimensionless turbulent kinetic energy k^* under different vegetation configurations: (a) near-surface plane (Z^* = 0.75); (b) near-bed plane (Z^* = 0.25).

3.3 Bed shear stress distribution

The bed shear stress was obtained from the wall shear stress calculated by the numerical model. To facilitate comparison among different vegetation configurations, the bed shear stress was normalized as:

$$\tau_b^* = \frac{\tau_b}{\rho U_0^2} \tag{4}$$

where τ_b^* is the dimensionless bed shear stress, τ_b is the dimensional bed shear stress obtained from the CFD simulation.

Figure 8 illustrates the spatial distribution of dimensionless bed shear stress τ_b^* on the mid-channel bar under different vegetation configurations, while Figure 9 summarizes the averaged bed shear stress variations in the head (H), middle (M), and tail (T) regions. Overall, the spatial pattern of bed shear stress corresponds well with the adjustments observed in the velocity and turbulent kinetic energy fields. The longitudinal vegetation configuration gradient primarily modifies the distribution of high-shear regions by redistributing the locations where vegetation-induced resistance

is exerted. Under bare-bar conditions (B), bed shear stress was mainly governed by bar morphology and local flow acceleration. High-shear regions were concentrated along the bar margins and lateral flow-conveyance zones, whereas relatively low values occurred within the bar interior and downstream tail region. After introducing uniform vegetation (G0), stem-scale flow disturbances generated localized high-shear zones around individual vegetation elements. Meanwhile, the reduction in central-region velocity caused decreased bed shear stress in some areas.

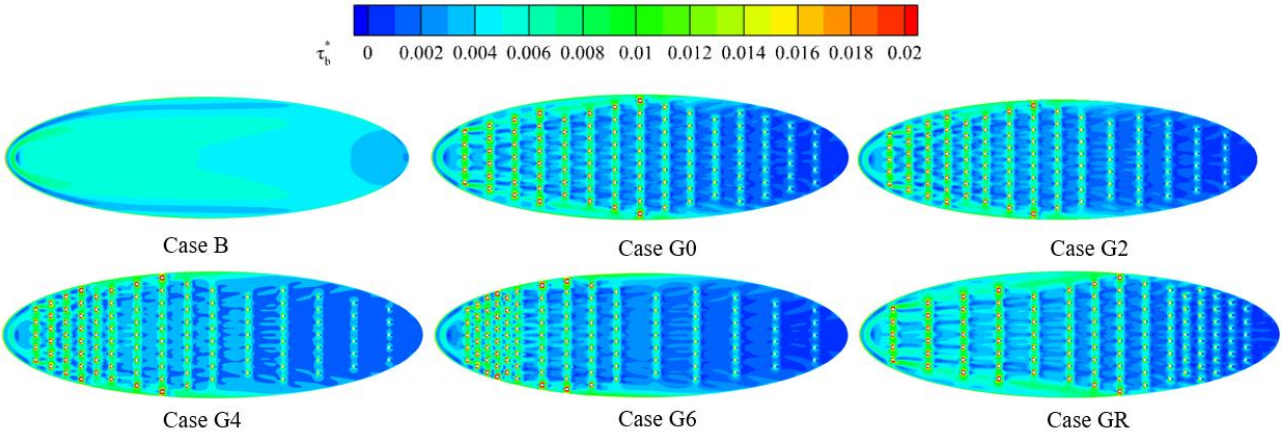

Fig. 8 Distributions of dimensionless bed shear stress τ_b^* on the mid-channel bar under different vegetation configurations

As shown in Figure 9, the averaged dimensionless bed shear stresses in the head, middle, and tail regions for G0 were approximately 0.00531, 0.00404, and 0.00200, respectively, exhibiting a gradual decrease along the flow direction. With increasing positive vegetation gradients (G0–G6), high bed shear stress regions progressively shifted toward the bar head. The reduced vegetation spacing at the bar head increased frontal resistance, thereby strengthening local velocity gradients and near-bed shear stress. According to Figure 9, as the gradient increased from 0 to 0.6, the averaged bed shear stress at the bar head increased from approximately 0.00531 to 0.00561, corresponding to an increase of approximately 5.65%. In contrast, the middle-region value decreased from 0.00404 to 0.00323 (approximately 20.05% reduction), and the tail-region value decreased from 0.00200 to 0.00158 (approximately 20.98% reduction). These results demonstrate that increasing the positive vegetation gradient does not uniformly enhance bed shear stress across the entire mid-channel bar. Instead, stronger shear stress is concentrated near the bar head, while persistent downstream shear is weakened. Compared with the bare-bar condition, G6 increased the head-region bed shear stress by approximately 8.56%, whereas the bed shear stress in the middle and tail regions decreased by approximately 34.42% and 63.46%, respectively. This indicates that denser vegetation at the bar head promotes earlier momentum adjustment upstream, while lateral flow redistribution reduces sustained

shear loading in downstream regions. The direction of vegetation gradients further influences the spatial distribution of bed shear stress. Under identical gradient magnitudes, G4 and GR exhibited distinct bed shear stress patterns. In G4, dense vegetation located at the bar head caused higher shear stresses to concentrate mainly in the upstream region, while the downstream region remained relatively low in bed shear stress. Conversely, GR placed dense vegetation at the bar tail, causing stronger resistance effects to persist into the middle and downstream regions. Figure 9 indicates that compared with G4, GR increased the averaged bed shear stress in the middle and tail regions by approximately 22.95% and 51.59%, respectively, demonstrating that gradient direction plays an important role in regulating the bed shear stress distribution.

In summary, the longitudinal vegetation configuration gradient regulates the longitudinal variation of bed shear stress by redistributing vegetation resistance along the streamwise direction. Positive gradients produce a response pattern characterized by enhanced shear stress at the bar head and reduced shear stress downstream, whereas reverse gradients extend high-shear regions toward downstream areas, thereby altering the potential erosion tendency of different parts of the mid-channel bar.

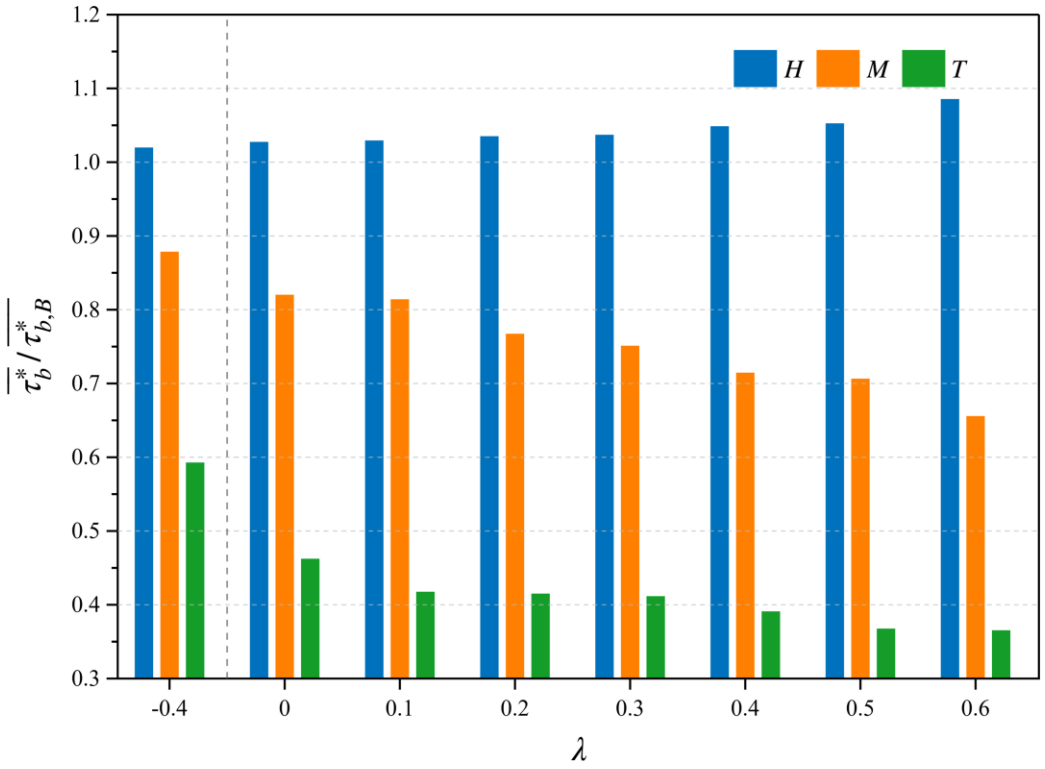

Fig. 9 Variation of averaged bed shear stress in the head, middle, and tail regions under different vegetation configurations

3.4 Turbulence-based sediment entrainment

Vegetation-induced turbulence plays an important role in controlling sediment mobility over vegetated bars. Although bed shear stress reflects the mean force acting on the bed, vegetation-generated turbulent fluctuations can provide additional disturbance to sediment particles. Therefore, the turbulence-based sediment entrainment model proposed by Xu et al. [48] was adopted to evaluate the sediment response under different vegetation configurations. The dimensionless near-bed turbulent kinetic energy was calculated as:

$$k_i^* = \frac{k_b}{(s-1)gd_{50}} \tag{5}$$

where k_b represents the turbulent kinetic energy extracted from the first computational cells adjacent to the bar surface.

The median grain size was determined based on field observations in the middle Yarlung Tsangpo River. According to Han et al. [49], sandy sediments dominate this region; therefore, d_{50} = 0.23mm was adopted. The dimensionless grain size was calculated as:

$$D^* = d_{50}\left[\frac{(s-1)g}{\nu^2}\right]^{1/3} \tag{6}$$

where s = 2.65 and ν = 1.0×10^{-6} m^2/s.

The critical Shields parameter was calculated following Soulsby and Whitehouse [50]:

$$\theta_c = \frac{0.3}{1+1.2D^*} + 0.055\left(1-e^{-0.02D^*}\right) \tag{7}$$

Following Xu et al. [49], the critical dimensionless turbulent kinetic energy was obtained from:

$$k_{itc}^* = \frac{\theta_c}{0.19} \tag{8}$$

The turbulence-driven sediment entrainment rate was calculated as:

$$E^* = \alpha_1 (D^*)^{\beta_1}\left(\frac{k_i^* - k_{itc}^*}{k_{itc}^*}\right)^{\gamma_1} \tag{9}$$

where $\alpha_1 = 1.5\times10^{-5}$, $\beta_1 = 1$, $\gamma_1 = 1$.

Figure 10 presents the spatial distribution of dimensionless sediment entrainment rate E^* under different longitudinal vegetation configurations. Overall, the distribution of E^* agrees well with that of near-bed dimensionless turbulent kinetic energy k_i^*, indicating that vegetation-induced turbulent

589 fluctuations play a key role in controlling sediment mobility over vegetated bars. Since E^* represents
590 the sediment response after the near-bed turbulent kinetic energy exceeds the critical threshold, its
591 spatial pattern provides direct information on potential erosion-prone regions.

592 Under the bare-bar condition (B), relatively high sediment entrainment potential is mainly
593 observed along the lateral margins and downstream convergence region of the bar. Without
594 vegetation resistance, accelerated flow and strong velocity gradients develop around these regions,
595 producing enhanced near-bed turbulence and increased sediment mobility. In contrast, the central part
596 of the bar exhibits relatively low E^* due to weak turbulent disturbance, indicating that sediment
597 activity on bare bars is primarily controlled by locally accelerated flow. After vegetation introduction,
598 the spatial pattern of sediment entrainment is substantially modified. High E^* regions become
599 concentrated around vegetation leading edges, vegetation boundaries, and lateral shear zones. This
600 distribution corresponds well with the enhanced near-bed turbulent kinetic energy, suggesting that
601 stem-scale wakes and vegetation-induced shear layers provide additional turbulent fluctuations for
602 sediment mobilization. Therefore, the turbulence-based criterion can better capture sediment
603 responses in vegetated regions than conventional approaches based solely on mean bed shear stress.
604 The longitudinal vegetation gradient further regulates the location of sediment entrainment. For
605 positive gradients (G0–G6), the high E^* region gradually shifts toward the upstream part of the bar
606 as vegetation density increases at the bar head. Dense upstream vegetation generates strong form
607 resistance, causing earlier flow adjustment and turbulence production. Meanwhile, the sparse
608 downstream vegetation reduces persistent turbulent disturbance, resulting in decreased sediment
609 entrainment potential in the downstream region. Overall, longitudinal vegetation configuration
610 regulates sediment mobility by controlling the spatial distribution of near-bed turbulent energy. Dense
611 vegetation at the bar head promotes rapid upstream adjustment and enhances downstream stability,
612 whereas dense vegetation at the bar tail prolongs turbulent disturbance and increases downstream
613 erosion potential. These findings highlight the importance of vegetation spatial organization in
614 controlling the stability of vegetated braided-river bars.

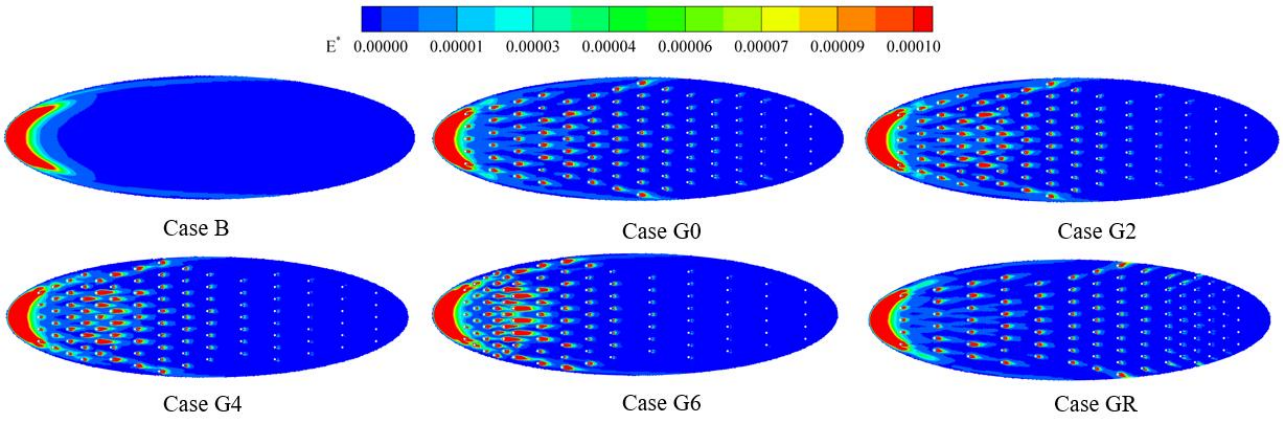

Fig. 10 Spatial distributions of turbulence-driven dimensionless sediment entrainment rate under different longitudinal vegetation configurations

4 Discussion

4.1 Vegetation-induced shear-layer development and turbulence redistribution

Previous studies have demonstrated that vegetation modifies flow structures mainly through vegetation-induced drag and momentum extraction, which reduce flow velocity within vegetated regions and alter momentum exchange with surrounding flow [26-27]. For finite vegetation patches, the contrast between vegetated and non-vegetated regions generates velocity gradients and shear layers along vegetation boundaries, which control lateral momentum transfer and turbulent exchange [33 , 37 , 51]. However, most previous studies have focused on isolated vegetation patches or uniformly distributed vegetation, whereas how vegetation spatial configuration within a vegetated mid-channel bar regulates bar-scale flow structures remains insufficiently understood. The present results reveal that vegetation within a mid-channel bar does not simply reduce flow velocity but reorganizes the bar-scale flow structure through resistance-induced flow redistribution. Compared with the bare-bar condition, vegetation establishment generated a low-momentum region within the elliptical vegetated area, where vegetation resistance extracted momentum from the mean flow.

To satisfy flow continuity, part of the incoming discharge was diverted toward both lateral sides of the vegetation patch, producing strong velocity gradients between the low-speed vegetated core and surrounding high-speed flow. Consequently, shear layers developed along the upper and lower boundaries of the elliptical vegetation zone, resulting in localized turbulence enhancement outside the vegetated core. This mechanism explains the high turbulent kinetic energy regions observed around the vegetation margins in Figure 7. After vegetation introduction, the maximum dimensionless

turbulent kinetic energy increased from approximately 0.015–0.020 under bare-bar conditions to 0.035–0.050 along the vegetation boundaries. Under the strongest positive gradient (G6), intensified upstream vegetation resistance further strengthened the leading-edge and lateral shear layers, with local turbulent kinetic energy reaching approximately 0.050–0.060. This process differs from turbulence generation associated with individual stem wakes. Although stem-scale wakes contribute to local turbulence production, the dominant bar-scale turbulence structure is controlled by the interaction between the vegetated low-momentum region and surrounding high-momentum flow. Therefore, vegetation configuration influences not only turbulence magnitude but also the spatial location of turbulence production zones. The schematic diagram in Figure 11 summarizes the mechanism revealed in this study.

4.2 Role of longitudinal vegetation configuration in regulating hydrodynamic adjustment

Vegetation quantity alone cannot fully explain the spatial variability of hydrodynamic responses, because vegetation arrangement determines where resistance is introduced along the flow direction. Previous studies have shown that vegetation density and spatial arrangement modify resistance characteristics through changes in frontal area distribution and wake interaction [23 ,25]. The present study extends this understanding by demonstrating that longitudinal vegetation gradients regulate the location and evolution of resistance within vegetated mid-channel bars. Under positive vegetation gradients, dense vegetation concentrated at the bar head increased upstream resistance and promoted earlier momentum adjustment. The resulting flow deceleration and lateral diversion occurred closer to the upstream region, causing the shear layers and turbulence production zones to develop earlier. Meanwhile, increased vegetation spacing toward the bar tail reduced downstream resistance, facilitating momentum exchange between lateral high-speed flows and the wake region. In contrast, the reverse-gradient configuration shifted dense vegetation toward the downstream region. Although the total vegetation quantity remained identical, the downstream concentration of resistance prolonged the influence of vegetation on the flow field, delayed central-flow recovery, and maintained enhanced turbulence in the downstream region. These results indicate that longitudinal vegetation configuration controls the timing and location of hydrodynamic adjustment rather than simply changing the overall resistance magnitude. Therefore, vegetation-induced hydrodynamic effects should be interpreted from a spatial perspective. The same vegetation coverage can produce substantially different flow responses when the resistance distribution along the bar is modified. This finding highlights that vegetation configuration represents an independent control factor for ecohydraulic processes in braided-river bars.

4.3 Influence on braided-river bar stability and limitations

Vegetation restoration in braided rivers is commonly evaluated based on vegetation coverage, biomass, or establishment area. However, the present results indicate that spatial organization of vegetation is also critical for regulating hydrodynamic processes. The longitudinal arrangement of vegetation determines the position of high-resistance zones, shear-layer development, turbulent energy redistribution, and bed shear stress patterns within vegetated bars. Dense vegetation located at the bar head can induce early flow adjustment and reduce persistent downstream hydraulic disturbance, whereas downstream concentration of vegetation resistance may maintain stronger turbulence and shear effects in downstream regions. These differences may influence sediment redistribution pathways and the long-term stability of vegetated bars. These findings complement previous studies emphasizing vegetation effects on channel stabilization by demonstrating that not only vegetation presence but also vegetation spatial configuration plays an important role in controlling braided-river bar hydrodynamics [15]. Considering vegetation arrangement together with vegetation quantity may provide a more comprehensive framework for understanding vegetation–flow interactions in dynamic braided-river systems.

It should be noted that the present study was conducted under fixed-bed conditions and primarily focused on hydrodynamic responses induced by longitudinal vegetation configurations, without considering long-term flow–sediment interactions. In natural braided-river environments, vegetation growth, sediment deposition, and channel-bed adjustment interact through complex coupled processes. Therefore, future studies should incorporate movable-bed numerical models, long-term field observations, and vegetation succession dynamics to further investigate the long-term impacts of different vegetation spatial configurations on bar evolution and channel morphological adjustment.

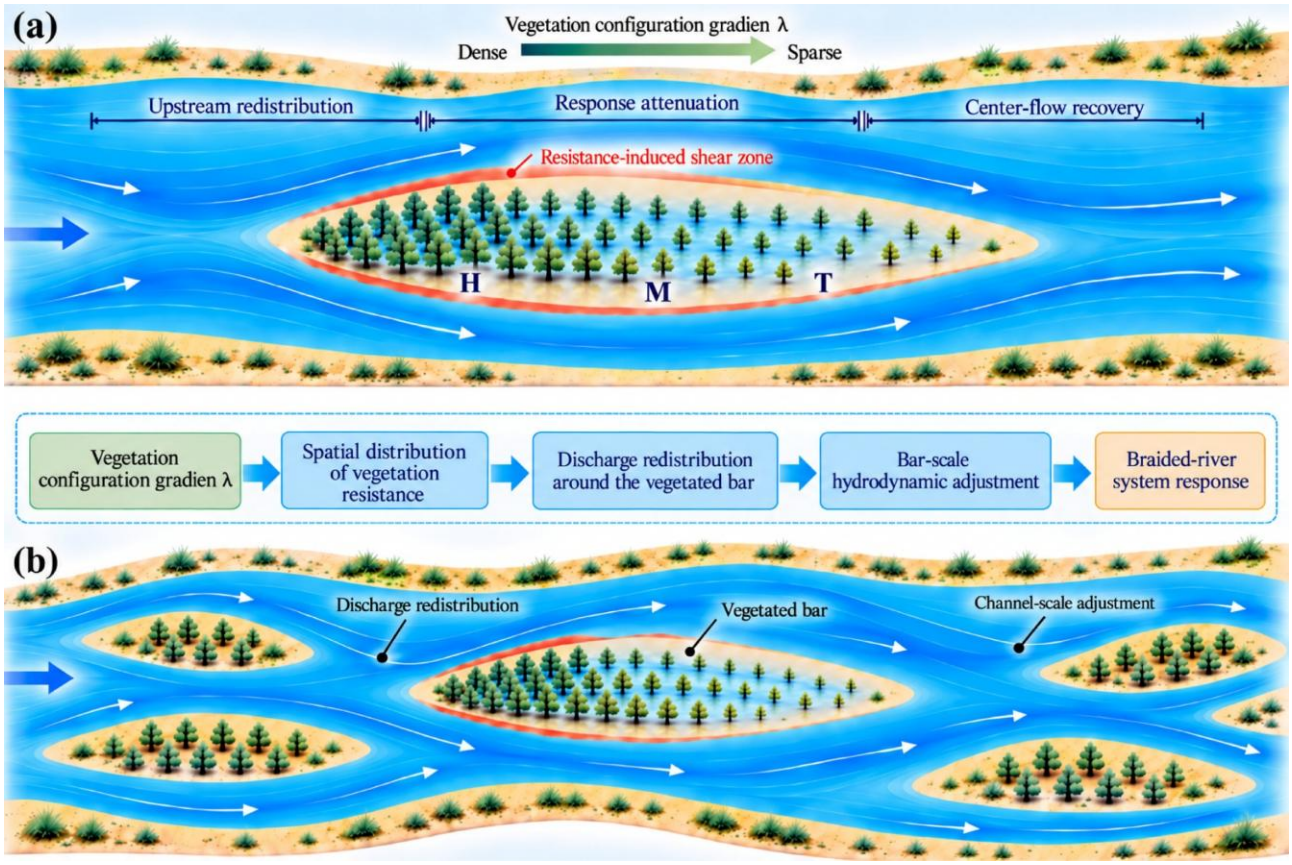

Fig. 11 Schematic diagram of hydrodynamic response mechanisms of vegetated mid-channel bars in braided rivers under longitudinal vegetation configuration gradients: (a) hydrodynamic response mechanism at the scale of an individual vegetated mid-channel bar; (b) flow partitioning adjustment response induced by vegetated mid-channel bars in braided rivers.

5 Conclusions

Using a typical vegetated mid-channel bar in the middle Yarlung Tsangpo River on the Tibetan Plateau as a prototype, this study developed a three-dimensional hydrodynamic model to investigate the effects of longitudinal vegetation configuration gradients on bar-scale hydrodynamic processes. While maintaining identical vegetation amount, coverage extent, and transverse arrangement, only the longitudinal distribution of vegetation spacing was modified. The main conclusions are summarized as follows:

(1) This study demonstrates that longitudinal vegetation configuration is an important factor regulating the hydrodynamic response of vegetated mid-channel bars, even under identical vegetation quantity and coverage. Vegetation establishment reduces momentum within the vegetated region and redistributes flow toward lateral conveyance zones, forming a low-velocity core within the elliptical

vegetation patch and accelerated flow along its margins. Positive vegetation gradients, with denser vegetation at the bar head and sparser vegetation at the bar tail, promote earlier flow adjustment and lateral flow diversion, whereas reverse gradients prolong downstream resistance effects.

(2) Longitudinal vegetation configuration regulates turbulence structures primarily through the development and relocation of vegetation-induced shear layers. Compared with the bare-bar condition, vegetation generates strong velocity gradients between the low-momentum vegetated core and surrounding high-speed flow, producing shear layers and high turbulent kinetic energy zones along both sides of the elliptical vegetation patch. Increasing positive gradients strengthen upstream shear-layer development and shift turbulence production toward the bar head, whereas reverse gradients maintain stronger downstream turbulent activity.

(3) Vegetation configuration redistributes near-bed hydrodynamic forcing by modifying the spatial distribution of bed shear stress and turbulent energy. Compared with uniform vegetation, the strongest positive gradient increased the averaged bed shear stress at the bar head by 5.65% but decreased that in the middle and tail regions by 20.05% and 20.98%, respectively. The turbulence-based sediment entrainment analysis further revealed that vegetation configuration influenced sediment mobility by modifying the spatial distribution of near-bed turbulent kinetic energy and sediment entrainment potential, with enhanced sediment response mainly occurring in regions affected by vegetation-induced shear layers.

Collectively, this study highlights that vegetation spatial configuration represents an independent control factor for vegetated braided-river bar stability. Beyond vegetation quantity, the longitudinal arrangement of vegetation determines the spatial distribution of resistance, shear-layer development, turbulent energy production, and sediment mobility. These findings provide new insights into vegetation–flow–sediment interactions and improve understanding of hydrodynamic adjustment processes in vegetated braided-river systems.

Acknowledgments

This study was supported by the National Natural Science Foundation of China (Grant Nos. 52479073 and 52509109).

Conflict of interest

All authors declare that there are no other competing interests.

References

[1] Ashmore, P.E., 2013. Morphology and dynamics of braided rivers. In: Shroder, J.F. (Ed.), Treatise on Geomorphology, vol. 9. Academic Press, San Diego, pp. 289–312. https://doi.org/10.1016/B978-0-12-374739-6.00242-6.

[2] Liu, Z., Zhao, W., 2001. Shifting-sand control in central Tibet. Ambio 30 (6), 376–380. https://doi.org/10.1579/0044-7447-30.6.376.

[3] Liao, C., Liu, B., Xu, Y., Li, H., 2019. Effect of topography and protecting barriers on revegetation of sandy land, Southern Tibetan Plateau. Sci. Rep. 9, 6501. https://doi.org/10.1038/s41598-019-43034-8.

[4] Liao, C., Li, H., Lv, G., Tian, J., Xu, Y., 2020. Effects of ecological restoration on soil properties of the aeolian sandy land around Lhasa, southern Tibetan Plateau. Ecosphere 11 (1), e03009. https://doi.org/10.1002/ecs2.3009.

[5] Zhang, B., Xiong, D., Tang, Y., Liu, L., 2022. Land surface roughness impacted by typical vegetation restoration projects on aeolian sandy lands in the Yarlung Zangbo River valley, southern Tibetan Plateau. Int. Soil Water Conserv. Res. 10 (1), 109–118. https://doi.org/10.1016/j.iswcr.2021.06.001.

[6] You, Y.C., Li, Z.W., Hu, X.Y., 2023. Impacts of artificial plantation encroachment on bar stability of braided channel in the middle Yarlung Tsangpo River. J. Sediment Res. 48 (1), 26–32 [in Chinese]. https://doi.org/10.16239/j.cnki.0468-155x.2023.01.005.

[7] Ma, J., Li, Z., Cheng, Y., You, Y., Yao, W., 2026. Hydrodynamic effects of riparian vegetation in an anabranching-confined transition reach in the middle Yarlung Tsangpo River. Int. J. Sediment Res. 41 (4), 561–576. https://doi.org/10.1016/j.ijsrc.2026.03.003.

[8] Corenblit, D., Tabacchi, E., Steiger, J., Gurnell, A.M., 2007. Reciprocal interactions and adjustments between fluvial landforms and vegetation dynamics in river corridors: A review of complementary approaches. Earth-Sci. Rev. 84 (1–2), 56–86. https://doi.org/10.1016/j.earscirev.2007.05.004.

[9] Camporeale, C., Perucca, E., Ridolfi, L., Gurnell, A.M., 2013. Modeling the interactions between river morphodynamics and riparian vegetation. Rev. Geophys. 51 (3), 379–414. https://doi.org/10.1002/rog.20014.

[10] Gurnell, A.M., Petts, G.E., Hannah, D.M., Smith, B.P.G., Edwards, P.J., Kollmann, J., Ward, J.V., Tockner, K., 2001. Riparian vegetation and island formation along the gravel-bed Fiume Tagliamento, Italy. Earth Surf. Process. Landf. 26 (1), 31–62. https://doi.org/10.1002/1096-9837(200101)26:1<31::AID-ESP155>3.0.CO;2-Y.

[11] Gurnell, A.M., 2014. Plants as river system engineers. Earth Surf. Process. Landf. 39 (1), 4–25. https://doi.org/10.1002/esp.3397.

[12] Gran, K., Paola, C., 2001. Riparian vegetation controls on braided stream dynamics. Water Resour. Res. 37 (12), 3275–3283. https://doi.org/10.1029/2000WR000203.

[13] Tal, M., Paola, C., 2007. Dynamic single-thread channels maintained by the interaction of flow and vegetation. Geology 35 (4), 347–350. https://doi.org/10.1130/G23260A.1.

[14] Murray, A.B., Paola, C., 2003. Modelling the effect of vegetation on channel pattern in bedload rivers. Earth Surf. Process. Landf. 28 (2), 131–143. https://doi.org/10.1002/esp.428.

[15] Tal, M., Paola, C., 2010. Effects of vegetation on channel morphodynamics: Results and insights from laboratory experiments. Earth Surf. Process. Landf. 35 (9), 1014–1028. https://doi.org/10.1002/esp.1908.

[16] Eaton, B.C., Millar, R.G., Davidson, S., 2010. Channel patterns: Braided, anabranching, and single-thread. Geomorphology 120 (3–4), 353–364. https://doi.org/10.1016/j.geomorph.2010.04.010.

[17] Gurnell, A.M., Bertoldi, W., Corenblit, D., 2012. Changing river channels: The roles of hydrological processes, plants and pioneer fluvial landforms in humid temperate, mixed load, gravel bed rivers. Earth-Sci. Rev. 111 (1–2), 129–141. https://doi.org/10.1016/j.earscirev.2011.11.005.
[18] Ricardo, A.M., Franca, M.J., Ferreira, R.M.L., 2016. Turbulent flows within random arrays of rigid and emergent cylinders with varying distribution. *Journal of Hydraulic Engineering* 142(9), 04016022. https://doi.org/10.1061/(ASCE)HY.1943-7900.0001151
[19] Yagci, O., Özgur Kirca, V.S., Kitsikoudis, V., Wilson, C.A.M.E., Furkan Celik, M., Sertkan, C., 2024. Experimental study on influence of different patterns of an emergent vegetation patch on the flow field and scour/deposition processes in the wake region. *Water Resources Research* 60, e2023WR034978. https://doi.org/10.1029/2023WR034978.
[20] Nepf, H.M., 1999. Drag, turbulence, and diffusion in flow through emergent vegetation. Water Resour. Res. 35 (2), 479–489. https://doi.org/10.1029/1998WR900069.
[21] Baptist, M.J., Babovic, V., Rodríguez Uthurburu, J., Keijzer, M., Uittenbogaard, R.E., Mynett, A., Verwey, A., 2007. On inducing equations for vegetation resistance. J. Hydraul. Res. 45 (4), 435–450. https://doi.org/10.1080/00221686.2007.9521778.
[22] Luhar, M., Nepf, H.M., 2013. From the blade scale to the reach scale: A characterization of aquatic vegetative drag. Adv. Water Resour. 51, 305–316. https://doi.org/10.1016/j.advwatres.2012.02.002.
[23] Tanino, Y., Nepf, H.M., 2008. Laboratory investigation of mean drag in a random array of rigid, emergent cylinders. J. Hydraul. Eng. 134 (1), 34–41. https://doi.org/10.1061/(ASCE)0733-9429(2008)134:1(34).
[24] Etminan, V., Lowe, R.J., Ghisalberti, M., 2017. A new model for predicting the drag exerted by vegetation canopies. Water Resour. Res. 53 (4), 3179–3196. https://doi.org/10.1002/2016WR020090.
[25] Busari, A.O., Li, C.W., 2016. Bulk drag of a regular array of emergent blade-type vegetation stems under gradually varied flow. J. Hydro-Environ. Res. 12, 59–69. https://doi.org/10.1016/j.jher.2016.02.003.
[26] Nepf, H.M., Vivoni, E.R., 2000. Flow structure in depth-limited, vegetated flow. J. Geophys. Res.: Oceans 105 (C12), 28547–28557. https://doi.org/10.1029/2000JC900145.
[27] Nepf, H.M., 2012. Flow and transport in regions with aquatic vegetation. Annu. Rev. Fluid Mech. 44, 123–142. https://doi.org/10.1146/annurev-fluid-120710-101048.
[28] Västilä, K., Järvelä, J., 2014. Modeling the flow resistance of woody vegetation using physically based properties of the foliage and stem. Water Resour. Res. 50 (1), 229–245. https://doi.org/10.1002/2013WR013819.
[29] Rominger, J.T., Nepf, H.M., 2011. Flow adjustment and interior flow associated with a rectangular porous obstruction. J. Fluid Mech. 680, 636–659. https://doi.org/10.1017/jfm.2011.199.
[30] Liu, C., Shan, Y., 2019. Analytical model for predicting the longitudinal profiles of velocities in a channel with a model vegetation patch. J. Hydrol. 576, 561–574. https://doi.org/10.1016/j.jhydrol.2019.06.076.
[31] Liu, C., Shan, Y., Sun, W., Yan, C., Yang, K., 2020. An open channel with an emergent vegetation patch: Predicting the longitudinal profiles of velocities based on exponential decay. J. Hydrol. 582, 124429. https://doi.org/10.1016/j.jhydrol.2019.124429.
[32] Ben Meftah, M., Mossa, M., 2016. Partially obstructed channel: Contraction ratio effect on the flow hydrodynamic structure and prediction of the transversal mean velocity profile. J. Hydrol. 542, 87–100. https://doi.org/10.1016/j.jhydrol.2016.08.057.

[33] White, B.L., Nepf, H.M., 2007. Shear instability and coherent structures in shallow flow adjacent to a porous layer. J. Fluid Mech. 593, 1–32. https://doi.org/10.1017/S0022112007008415.
[34] Ghisalberti, M., Nepf, H.M., 2002. Mixing layers and coherent structures in vegetated aquatic flows. J. Geophys. Res.: Oceans 107 (C2), 3011. https://doi.org/10.1029/2001JC000871.
[35] Ghisalberti, M., Nepf, H.M., 2004. The limited growth of vegetated shear layers. Water Resour. Res. 40 (7), W07502. https://doi.org/10.1029/2003WR002776.
[36] Chen, Z., Ortiz, A., Zong, L., Nepf, H.M., 2012. The wake structure behind a porous obstruction and its implications for deposition near a finite patch of emergent vegetation. Water Resour. Res. 48 (9), W09517. https://doi.org/10.1029/2012WR012224.
[37] Zong, L., Nepf, H.M., 2012. Vortex development behind a finite porous obstruction in a channel. J. Fluid Mech. 691, 368–391. https://doi.org/10.1017/jfm.2011.479.
[38] Zong, L., Nepf, H.M., 2010. Flow and deposition in and around a finite patch of vegetation. Geomorphology 116 (3–4), 363–372. https://doi.org/10.1016/j.geomorph.2009.11.020.
[39] Follett, E.M., Nepf, H.M., 2012. Sediment patterns near a model patch of reedy emergent vegetation. Geomorphology 179, 141–151. https://doi.org/10.1016/j.geomorph.2012.08.006.
[40] Ortiz, A.C., Ashton, A., Nepf, H.M., 2013. Mean and turbulent velocity fields near rigid and flexible plants and the implications for deposition. J. Geophys. Res.: Earth Surf. 118 (4), 2585–2599. https://doi.org/10.1002/2013JF002858.
[41] Liu, C., Nepf, H.M., 2016. Sediment deposition within and around a finite patch of model vegetation over a range of channel velocity. Water Resour. Res. 52 (1), 600–612. https://doi.org/10.1002/2015WR018249.
[42] Savio, M., Vettori, D., Biggs, H., Zampiron, A., Cameron, S.M., Stewart, M., Soulsby, C., Nikora, V., 2023. Hydraulic resistance of artificial vegetation patches in aligned and staggered configurations. J. Hydraul. Res. 61 (2), 220–232. https://doi.org/10.1080/00221686.2023.2180445.
[43] Kitsikoudis, V., Yagci, O., Kirca, V.S.O., 2020. Experimental analysis of flow and turbulence in the wake of neighboring emergent vegetation patches with different densities. Environ. Fluid Mech. 20 (6), 1417–1439. https://doi.org/10.1007/s10652-020-09746-6.
[44] Bae, I., Ji, U., Järvelä, J., Västilä, K., 2024. Blockage effect of emergent riparian vegetation patches on river flow. J. Hydrol. 635, 131197. https://doi.org/10.1016/j.jhydrol.2024.131197.
[45] Vandenbruwaene, W., Temmerman, S., Bouma, T.J., Klaassen, P.C., de Vries, M.B., Callaghan, D.P., van Steeg, P., Dekker, F., van Duren, L.A., Martini, E., Balke, T., Biermans, G., Schoelynck, J., Meire, P., 2011. Flow interaction with dynamic vegetation patches: Implications for biogeomorphic evolution of a tidal landscape. J. Geophys. Res.: Earth Surf. 116 (F1), F01008. https://doi.org/10.1029/2010JF001788.
[46] Liu, M., Huai, W., Tang, H., Wang, Y., Yuan, S., 2024. Numerical study of mean and turbulent flow adjustments in open channels with limited near-bank vegetation patches. Phys. Fluids 36 (9), 095117. https://doi.org/10.1063/5.0222692.
[47] Nandi, K.K., Kakati, R., Dutta, S., Khatua, K.K., 2024. Exploring the influence of vegetated mid-channel bar on flow and turbulence in bifurcated channels: An experimental approach. *Advances in Water Resources* 189, 104727. https://doi.org/10.1016/j.advwatres.2024.104727
[48] Xu, Y., Li, D., Nepf, H., 2022. Sediment pickup rate in bare and vegetated channels. *Geophysical Research Letters* 49, e2022GL101279. https://doi.org/10.1029/2022GL101279.
[49] Han, K., Sun, J., Li, Z., Lin, B., Yang, Y., Huang, Z., 2021. Grain-size and geometry characteristics of braided rivers in a wide plateau valley. *Journal of Hydroelectric Engineering* 40(12), 1–11. https://doi.org/10.11660/slfdxb.20211201.

[50] Soulsby, R.L., Whitehouse, R.J.S., 1997. Threshold of sediment motion in coastal environments. Proceedings of the Pacific Coasts and Ports '97 Conference, University of Canterbury, Christchurch, New Zealand, 149–154.
[51] White, B.L., Nepf, H.M., 2008. A vortex-based model of velocity and shear stress in a partially vegetated channel. *Water Resources Research* 44, W01406. https://doi.org/10.1029/2007WR006505.